Catalysis Today 136 (2008) 243–248

Contents lists available at ScienceDirect

Catalysis Today

journal homepage: www.elsevier.com/locate/cattod

Hydrocarbon steam reforming on Ni alloys at solid oxide fuel cell operating conditions

Eranda Nikolla, Johannes W. Schwank, Suljo Linic *

Department of Chemical Engineering, University of Michigan, 2300 Hayward Street, Ann Arbor, MI 48109, United States

ARTICLE INFO

Keywords:
SOFC
DFT
Steam reforming
Carbon poisoning
Alloys

ABSTRACT

We demonstrate that supported Sn/Ni alloy catalyst is more resistant to deactivation via carbon deposition than supported monometallic Ni catalyst in steam reforming of isooctane at moderate steam to carbon ratios, irrespective of the average size of metal particles and the metal loading. The experiments were performed for average diameters of catalytic particles ranging from 30 to 500 nm and for the loading of active material ranging from 15 to 44 wt% with respect to the total mass of catalyst. The steam reforming reactions were performed at conditions that are consistent with typical solid oxide fuel cell (SOFC) operating conditions. DFT calculations show that the reasons for the enhanced carbon-tolerance of Sn/Ni compared to monometallic Ni are high propensity of Sn/Ni to oxidize carbon and lower driving force to form carbon deposits on low-coordinated metal sites.

1. Introduction

Steam reforming is a catalytic process for commercial hydrogen production. It is an endothermic reaction that involves the conversion of hydrocarbons and water into hydrogen and CO (1). In a catalytic reactor, this reaction is accompanied by the slightly exothermic water gas shift (WGS) reaction (2), which converts CO and steam into CO_2 and hydrogen.

$$C_nH_m + nH_2O \Rightarrow nCO + \left(\frac{n+m}{2}\right)H_2 \quad (\Delta H_{298} > 0) \tag{1}$$

$$CO + H_2O \Leftrightarrow CO_2 + H_2 \quad (\Delta H_{298} = -41.2\,\text{kJ/mol}) \tag{2}$$

Steam reforming is also important in direct utilization of hydrocarbons in solid oxide fuel cells (SOFCs) [1–6]. In SOFCs, H_2 is electrochemically oxidized at the three-phase boundary (TPB) – TPB is the region where anode and electrolyte are in direct contact with each other – resulting in the formation of steam, which then internally reacts with the incoming fuel via steam reforming to form hydrogen and CO. Most steam reforming catalysts and SOFC anode electro-catalysts contain Ni metal supported on an oxide [7–9]. Ni is the preferred catalytic material due to its excellent thermal and electronic characteristics, low cost, and high chemical activity. The ceramic oxide supports offer superior mechanical and thermal stability.

One of the main issues with hydrocarbon steam reforming over supported Ni catalysts is the deactivation of Ni due to the formation of carbon deposits. The carbon-induced deactivation of Ni has been studied extensively [7,10–26]. For example, Rostrup-Nielsen and coworkers have reported that steam reforming of various liquid fuels on Ni leads to rapid catalyst deactivation due to the formation of encapsulating, whisker-like, or pyrolytic carbon on the catalyst [7,8,13]. Multiple studies have been performed to elucidate the mechanism of the formation and growth of carbon deposits on Ni [11,17,20]. For example, in situ transmission electron microscopy (TEM) studies have shown that during methane decomposition on $Ni/MgAl_2O_4$ carbon nucleates at the under-coordinated Ni surface sites [17]. It was also shown that the extended carbon structures are formed in the process of the diffusion of C atoms and fragments on the surface of Ni and their attachment to the carbon nucleation centers on the low-coordinated Ni sites.

It is possible to circumvent the carbon-induced deactivation of Ni by increasing the steam to carbon ratio (S/C) in the feed. While the presence of additional steam enhances the oxidation and removal of carbon in the form of CO and CO_2, it also increases the mass flow rate through the reformer thus escalating the size of the reactor and capital cost. In addition, a substantial energy input is required to vaporize water and increase its temperature to the operating conditions. Another disadvantage of the high inlet steam

* Corresponding author. Tel.: +1 734 647 7984; fax: +1 734 764 7453.
E-mail address: linic@umich.edu (S. Linic).

Abbreviations: DFT, density functional theory; TEM, transmission electron microscopy; STEM, scanning transmission electron microscopy; SOFC, solid oxide fuel cell; YSZ, 8 mol% yttria stabilized zirconia; EELS, electron energy loss spectroscopy; SEM, scanning electron microscopy; EDS, energy dispersive X-ray spectroscopy; XPS, X-ray photoelectron spectroscopy; XRD, X-ray diffraction.

0920-5861/$ – see front matter © 2008 Elsevier B.V. All rights reserved.
doi:10.1016/j.cattod.2008.03.028

concentration is that it reduces the flexibility to control the outlet CO/H_2 ratio. This approach is also not optimal for SOFCs since an increase in inlet steam concentration results in a decrease in the energy density of reactants. The introduction of steam also requires additional SOFC components (i.e. a water tank, preheating system to vaporize water), adding complexity to the system design and integration.

In situ regeneration of the coked catalysts has also been explored to prevent irreversible carbon-induced deactivation [7,8]. In this process, non-aged, soft carbon, formed during steam reforming on Ni, is gasified by temporarily increasing the S/C ratio. The initial carbon formation on the catalyst is detected by performing a carbon balance on the system. The problem with this strategy is that, often, the formation of carbon deposits is rapid and even small amounts of carbon lead to the irreversible degradation of the active catalytic particles. This is especially problematic for SOFCs since the disintegration of the anode catalyst leads to the failure of the entire cell thus making the regeneration process impossible.

Another approach to prevent carbon deactivation is to develop catalysts that are inherently more carbon-tolerant than Ni [19,27–33]. For example, it has been suggested that metals such as Ru and Rh do not facilitate the formation of carbon deposits due to poor carbon solubility in these metals [13,34]. However, Ru and Rh are prohibitively expensive. It has also been shown that the negative effect of carbon can be alleviated by selectively poisoning the low-coordinated Ni sites (carbon nucleation centers are formed on these sites) with small amounts of sulfur [14,16]. Similarly, quantum chemical DFT calculations have predicted that Au/Ni surface alloys should exhibit an improved carbon-tolerance as compared to monometallic Ni [20,29]. These predictions have been verified experimentally. It has also been shown that Cu supported on ceria is a stable SOFC anode electro-catalyst for the internal utilization of hydrocarbons over SOFCs [35,36]. Compared to Ni-based electro-catalysts these materials are operated at lower temperatures due to the inferior thermal stability of Cu and ceria and thermal incompatibility of the ceria electro-catalyst and the 8 mol% yttria stabilized zirconia (YSZ) electrolyte. There are also reports in the patent literature suggesting that a large number of additives, including those mentioned below in the text (e.g. Sn), can be used to suppress the formation of carbon deposits on Ni [37].

We have previously reported that the Sn/Ni catalysts exhibit improved carbon-tolerance with respect to monometallic Ni in steam reforming of multiple hydrocarbons at moderate S/C ratios [28,38]. The studies were performed at external conditions that were consistent with the operation of SOFCs, i.e., the operating temperature was 1000–1100 K. Furthermore, the loading of the active metal material (Ni or Sn/Ni) was ~45 wt% with respect to the total catalyst (active material plus support) and the average diameter of catalytically active particles was ~0.5 μm. In this contribution we have expanded on the previous studies demonstrating that Sn/Ni catalysts are more resistant to carbon than monometallic Ni for a wide range of metal loadings and particle size.

2. Experimental

2.1. Catalyst synthesis

8 mol% Yttria stabilized zirconia was prepared via a standard co-precipitation method [28]. A mixture of yttrium nitrate ($Y(NO_3)_3{\cdot}6H_2O$) and zirconyl chloride ($ZrOCl_2{\cdot}2H_2O$) dissolved in deionized water was precipitated using a solution of ammonium hydroxide. After filtration and drying overnight, the precipitate was calcined at 1073 K for 2 h.

We have used two different strategies, incipient wetness and ball milling, to introduce Ni on the YSZ support. The main difference between these synthesis strategies is that they yielded metal particles with significantly different diameters. These two approaches are generally utilized in the synthesis of steam reforming catalysts (incipient wetness) and anode electro-catalysts for SOFCs (ball milling). Therefore, we refer to catalysts synthesized with the incipient wetness and ball milling techniques as steam reforming and SOFC anode catalysts, respectively.

The Ni/YSZ steam reforming catalyst was prepared by the incipient wetness technique. An equivalent of ~15 wt% of Ni with respect to the total amount of catalyst (Ni plus YSZ) in the form of $Ni(NiO_3)_3$ was dissolved in ethanol and sequentially impregnated on the YSZ support. The catalyst was calcined in air at 873 K for 2 h and then reduced using a gas mixture of 30% H_2/N_2 at 1073 K for 5 h. This procedure resulted in metal particles of ~30 nm, as measured by TEM and XRD, in diameter anchored on the support. The Sn/Ni/YSZ steam reforming catalyst was prepared by impregnating ~3 wt% of Sn, with respect to Ni, in the form of $SnCl_2{\cdot}4H_2O$ on the calcined NiO/YSZ sample. The appropriate amount of $SnCl_2{\cdot}4H_2O$ was dissolved in ethanol followed by sequential impregnation of the solution onto NiO/YSZ. The catalyst samples were then calcined again at 873 K for 2 h and reduced under a stream of 30% H_2/N_2 for 5 h at 1073 K.

SOFC anode catalyst was prepared by ball milling a mixture of 50 wt% YSZ and 50 wt% of NiO in methanol for 24 h. After drying, the powder was pressed into 13 mm diameter pellets at 5000 psi. The pellets were then sintered by ramping the temperature at 2 K/min to 1673 K and keeping them at this temperature for 4 h. The catalyst was further reduced at 1173 K for 5 h in a gas mixture of 30% H_2/N_2 to insure the full reduction of the pellets. This synthesis procedure yielded catalytic particles with ~0.5 μm diameter, as measured by TEM and XRD. The resulting catalysts had a Ni loading of 44 wt%. The Sn/Ni/YSZ SOFC anode catalyst was prepared by impregnating $SnCl_2{\cdot}4H_2O$ (~1 wt% with respect to Ni) on the sintered NiO/YSZ pellets via the incipient wetness technique. The pellets were dried overnight at 473 K and then reduced under a stream of 30% H_2/N_2 for 5 h at 1173 K. In our reactor studies we have tested these catalysts in the powder and pellet form. The powder was produced by mechanically crushing the pellets.

2.2. Reactor studies

The reactor experiments were conducted isothermally at 1073 K in a packed bed quartz reactor. The set-up included a set of mass flow controllers for gas delivery, a pair of thermocouples (inside and outside the reactor), as well as peristaltic and syringe pumps for liquid delivery. The reactor effluent was analyzed using a Varian gas chromatograph (Varian CP 3800) equipped with thermal conductivity detectors (TCD), a flame ionization detector (FID), and Hayesep P 80/100, Molsieve 13X 45/60, Hayesep R 80/100 and Molsieve 5A 45/60 columns. The mass of the catalysts and the total flow rate were varied to obtain a gas hourly space velocity (GHSV) of 0.05 mol/g-min in a reactor with the diameter of 0.5 in.

2.3. Scanning transmission electron microscopy (STEM), transmission electron microscopy (TEM), energy dispersive X-ray spectroscopy (EDS) and electron energy loss spectroscopy (EELS)

JEOL 2010F electron microscope was used for STEM, TEM, EDS and EELS studies. The instrument was operated at 200 kV under a pressure of 1.5×10^{-7} Torr. The instrument is equipped with a zirconated tungsten (1 0 0) thermal field emission tip filament and a Gatan Imaging Filter (GIF) for electron energy loss spectroscopy experiments. The lens was conditioned for a probe size of about

0.2 nm, with a convergence angle of 13 mrad and a collection angle of 40 mrad. The energy resolution (defined by the full width at half maximum of the zero loss peak) of the energy loss spectra is 1.5 eV at a dispersion of 0.3 eV per pixel.

2.4. Density functional theory (DFT)

The Dacapo pseudo-potentials plane wave code (http://www.camp.dtu.dk) was employed for all calculations. Our approach was to find a set of parameters that ensured the relative convergence, i.e., the convergence of the relative energies of various structures. With this set of parameters we have been able to reproduce various properties such as carbon atom adsorption energies, oxygen adsorption energies, graphene sheet adsorption energy on Ni(1 1 1), and activation barrier for the attachment of a C atom to the graphene sheet over Ni(1 1 1) reported previously by others [11,16,24]. For model systems with the (1 1 1) surface termination, we used a 3×3 supercell with four layers of metal atoms. We utilized 18 special Chadi-Cohen k-points to sample the Brillouin zone. The calculations for the (2 1 1) surface termination were performed using slabs with nine layers of metal organized in 1×3 supercells. Monkhorst-Pack mesh with a $3 \times 3 \times 1$ k-point grid was employed to sample the Brillouin zone. Adsorbates were adsorbed on one side of a slab. Approximately, 15 Å of vacuum separated the slabs, and a dipole-correction scheme was employed to electro-statically decouple the slabs. Electron exchange correlation effects were described using the generalized gradient approximation (GGA) with the Perdew–Wang 91 (PW91) functional [39,40]. Vanderbilt pseudo-potentials were employed to describe core electrons [41]. The density of valence electrons was determined self-consistently by iterative diagonalization of Kohn-Sham Hamiltonian using Pulay mixing of densities. The plane wave basis set used to describe the one-electron states was cut off at 350 eV. An electronic temperature (k_bT) of 0.1 was utilized during calculations with the final results extrapolated to 0 K. In the geometry optimization calculations on the (1 1 1) surface termination, the two top substrate layers and adsorbates were allowed to relax in the z direction. On the (2 1 1) termination, the two top substrate layers were allowed to relax in the x (normal to the direction if the step-edge) and z directions. The forces were minimized to 0.05 eV/A.

3. Results

We have previously reported a number of experimental and theoretical studies aimed at characterizing the Sn/Ni/YSZ catalyst [38]. These characterization studies indicated that the impregnation of Ni particles with a small amount of Sn results in the formation of Sn/Ni surface alloys. The surface alloy is characterized by Sn mixing with Ni in the surface layers of the particle. For example, DFT calculations showed that the free energy of formation for the Sn/Ni surface alloy is lower than the formation energy of other Sn/Ni structures, including Sn dissolved in Ni bulk or separated phases of pure Sn and Ni [38]. The predictions of DFT calculations have been verified experimentally [38]. For instance, we utilized X-ray photoelectron spectroscopy (XPS) to determine that the atomic concentration of Sn in the surface layers of the reduced Sn/Ni catalytic particles was ~25% for the Sn/Ni particles that contained ~1 wt% of Sn with respect to Ni. These particles were approximately 50 nm in diameter [28,38]. Furthermore, scanning electron energy loss spectroscopy measurements showed that Sn preferentially segregates towards the surface of Sn/Ni particles. For example, Fig. 1b and c shows the electron energy loss spectra corresponding to the Sn M-edge and Ni L-edge obtained for an electron beam focused on a region close to the boundary of a Sn/Ni particle and a region close to the center of the particle. Fig. 1b and c demonstrate that the ratio of the Sn M-edge to Ni L-edge is higher at the boundary of the particle and it decreases as the electron bean is moved closer to the center of the particle. These results provide further evidence that there is an enrichment of Sn close at the surface of the Sn/Ni particles. Furthermore, our energy dispersive X-ray spectroscopy and temperature programmed reduction (TPR) measurements also corroborated the results discussed above suggesting the formation of Sn/Ni surface alloy [28,38]. It is important to note that the amounts of Sn and Ni required to form the Sn/Ni surface alloys depends critically on the size of catalytic particles, i.e., on the particle surface to volume ratio. Large particles require less Sn with respect to Ni compared to smaller catalytic particles.

Fig. 2 shows the conversion of isooctane as a function of time in steam reforming of isooctane at a steam to carbon (S/C) ratio of 1.5 and an operating temperature of 1073 K for four different

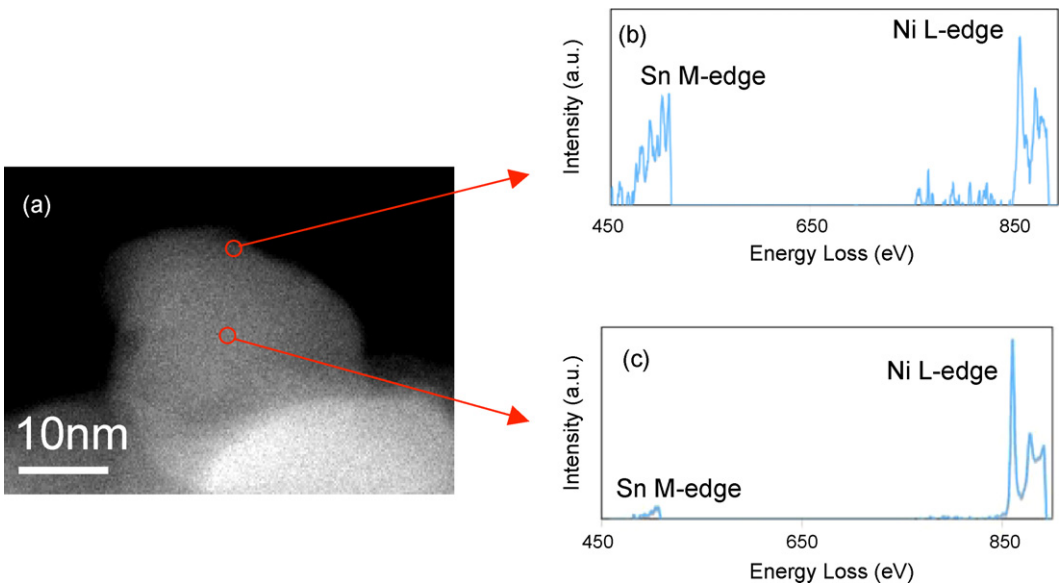

Fig. 1. (a) Scanning transmission electron micrograph (STEM) of a 3%Sn/15%Ni/YSZ (3 wt% of Sn with respect to Ni, 15 wt% of Ni with respect to the total catalyst) particle. Electron energy loss spectrum (EELS) of the Sn M-edge and Ni L-edge for an electron beam focused on (b) a region close to the boundary of the particle and (c) a region close to the center of the particle.

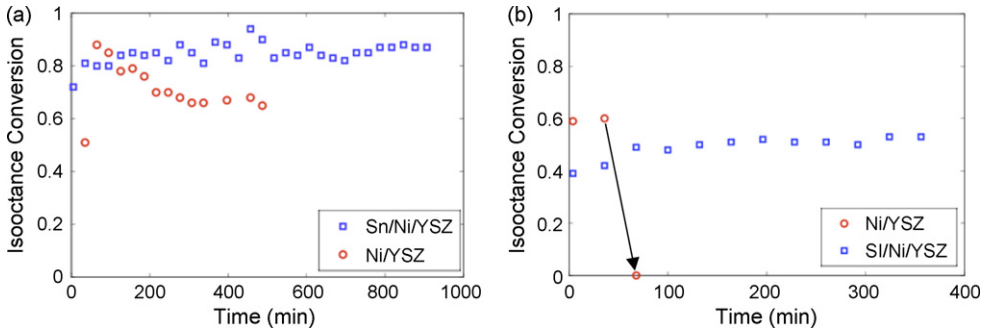

Fig. 2. Isooctane conversion in steam reforming of isooctane at S/C ratio of 1.5 and 1073 K for: (a) 15%Ni/YSZ catalyst (15 wt% of Ni with respect to the total catalyst) and a 3%Sn/15%Ni/YSZ catalyst (3 wt% of Sn with respect to Ni, 15 wt% of Ni with respect to the total catalyst). Both catalysts had an average metal particle diameter of ~30 nm, (b) 44%Ni/YSZ catalyst (44 wt% of Ni with respect to the total catalyst) and a 1%Sn/44%Ni/YSZ catalyst (1 wt% Sn with respect to Ni). Both catalysts had an average metal particle diameter ~500 nm.

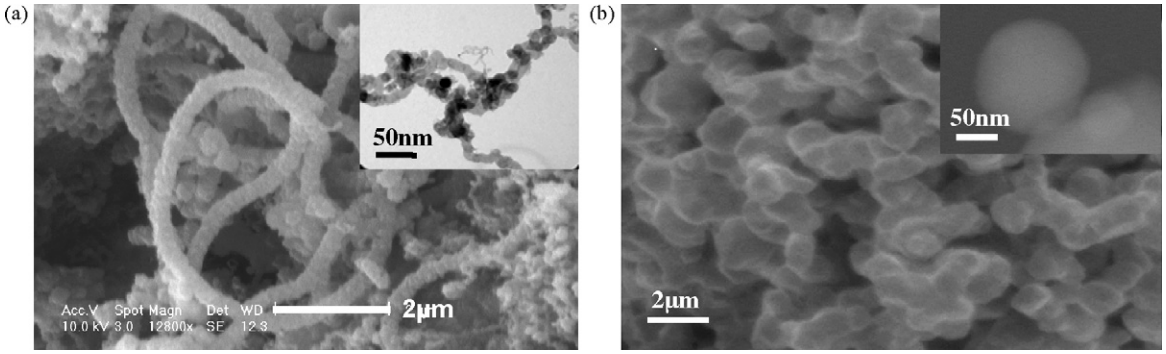

Fig. 3. (a) SEM and TEM (insert) images of a 44%Ni/YSZ catalyst after steam reforming of isooctane. This process resulted in the formation of carbon filaments. (b) SEM and STEM (insert) images for a 1%Sn/44%Ni/YSZ catalyst after steam reforming of isooctane. No carbon was detected on the catalyst.

catalysts: (1) 15%Ni/YSZ (15 wt% Ni loading with respect to the total catalyst (Ni and YSZ) and average particle diameter of 30 nm), (2) 3%Sn/15%Ni/YSZ (15 wt% Ni loading with respect to the total catalyst, 3 wt% Sn with respect to Ni, and average particle diameter of 30 nm), (3) 44%Ni/YSZ (44 wt% Ni with respect to the catalyst mass and an average particle diameter of 0.5 μm), and (4) 1%Sn/44%Ni/YSZ (44 wt% Ni with respect to Ni plus YSZ, 1 wt% of Sn with respect to Ni, and an average particle diameter of 0.5 μm). The procedures used to synthesize these catalysts are described above. Fig. 2 shows that the conversion of isooctane for both Sn/Ni/YSZ catalysts, irrespective of metal loading and average particle diameter, was stable for as long as the catalyst was kept on stream. The longest tests lasted for approximately 5 days. In contrast to the Sn/Ni/YSZ catalysts, the conversion of isooctane on monometallic Ni supported on YSZ deteriorated over time for both Ni/YSZ catalysts. The reactor tests also showed that the Ni/YSZ catalyst with smaller Ni particles (15%Ni/YSZ) was more resistant to carbon than the Ni/YSZ catalyst with larger metal particles (44%Ni/YSZ) for identical operating conditions. These observations have also been made by others and are generally attributed to the high energy of the carbon deposits, mainly carbon nano-fibers, formed in the process of catalyst deactivation [8,26,42,43]. The high energy of carbon deposits results in a lower driving force to form these deposits on smaller Ni particles compared to larger particles.

Electron microscopy studies performed on used Ni/YSZ catalysts showed that the deactivation of Ni/YSZ was a consequence of the formation of carbon deposits which led to the disintegration of Ni particles. For example, Fig. 3a shows a scanning electron micrograph and a transmission electron micrograph of a used 44%Ni/YSZ catalyst. It is clear that the catalytic particles were completely covered by carbon. Fig. 3b shows SEM and STEM images of used 1%Sn/44%Ni/YSZ. Unlike for the Ni/YSZ catalyst, no carbon deposits were detected on 1%Sn/44%Ni/YSZ. We have also utilized XPS to further characterize the used catalysts [28,38]. These measurements showed that a substantial amount of graphitic carbon was formed on the 44%Ni/YSZ catalyst during isooctane steam reforming. On the other hand no significant carbon deposition was detected on the 1%Sn/44%Ni/YSZ catalyst. Similar results showing that monometallic Ni catalysts deactivated due to the formation of extended carbon structures on Ni were also obtained for the catalytic particles with smaller diameter and metal loading, mainly 15%Ni/YSZ and 3%Sn/15%Ni/YSZ catalysts.

4. Discussion

The results presented above show that, irrespective of metal loading or the size of catalytic particles, the Sn/Ni catalysts are more carbon-tolerant than monometallic Ni in steam reforming of

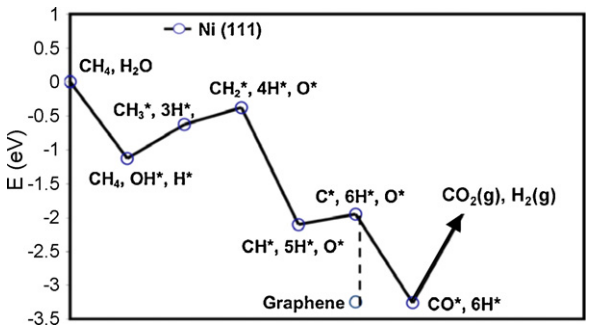

Fig. 4. (a) DFT-calculated reaction energies for elementary steps in steam reforming of methane on Ni(1 1 1).

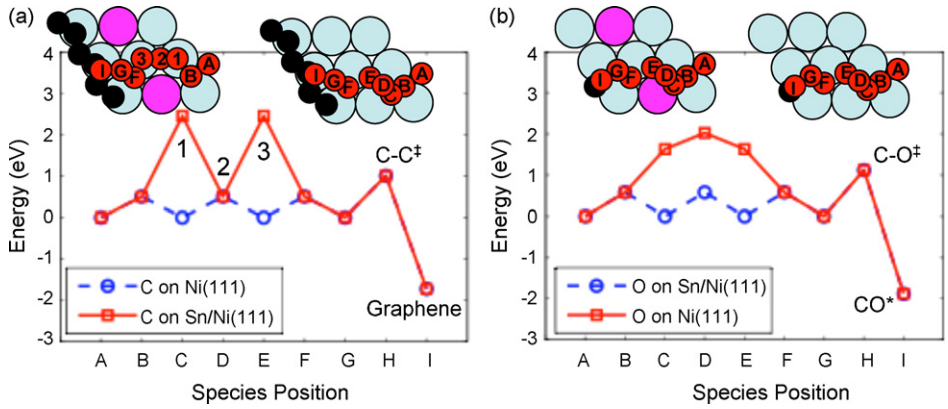

Fig. 5. (a) DFT-calculated potential energy surfaces for C–C bond formation on Ni(1 1 1) and Sn/Ni(1 1 1). Inserts show the lowest energy pathways for the attachment of a C atom to a carbon nucleation center (modeled as a chain of carbon atoms) on the two surfaces shown in the insert, (b) C–O bond formation on Ni(1 1 1) and Sn/Ni(1 1 1). Inserts show the lowest energy pathways for the two surfaces shown in the insert. Ni is depicted as large blue (light) atom, Sn as a large purple atom, carbon chain as a chain of small black atoms.

isooctane at moderate S/C ratios. These observations suggest that Sn/Ni could be a more carbon-resistant alternative to Ni for catalytic hydrogen production from hydrocarbons and for the direct utilization of hydrocarbon fuels in SOFCs. In the next paragraphs, we will identify the underlying molecular principles, grounded in first principles DFT calculations, which could explain the improved carbon-tolerance of Sn/Ni as compared to mono-metallic Ni.

It is generally accepted that at high operating temperature (1000–1200 K) hydrocarbon molecules rapidly decompose on Ni forming adsorbed carbon fragments and hydrogen atoms [20]. In addition, steam activation results in the formation of adsorbed O* and OH*. For example, in Fig. 4 we show the reaction energies, calculated using DFT, for various elementary steps involved in steam reforming of methane on Ni(1 1 1). The figure shows that on Ni(1 1 1) the adsorbed CH_x fragments with the lowest energy are C* and CH*. Our DFT calculations also indicate that there exists a strong thermodynamic diving force for C* and CH* to further react with O* or OH* to form adsorbed CO*, or to react with each other to form graphitic carbon deposits. It is important to recognize that the formation of CO on Ni provides a pathway for the removal of the C atoms from the catalyst surface in the process of further oxidation of CO to form gas phase CO_2. On the other hand the formation of carbon deposits on Ni results in the deactivation of the Ni catalyst.

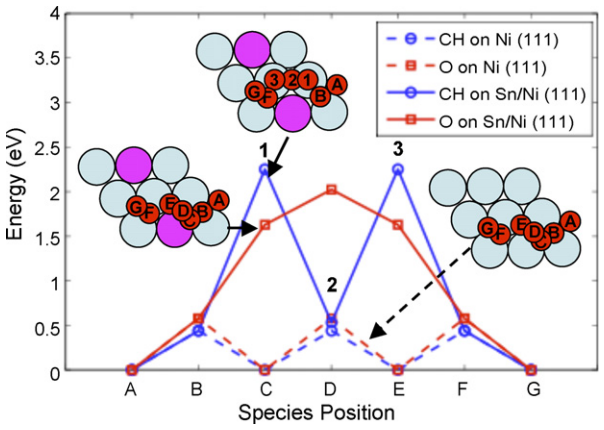

Fig. 6. DFT-calculated diffusion pathways for O and CH on Ni(1 1 1) and Sn/Ni(1 1 1). Inserts show the lowest energy pathways. On Ni(1 1 1), the lowest energy pathway for both. O and CH, is the ABCDEFG path. On the Sn/Ni(1 1 1) model system, the lowest energy pathway for O is the ABCDEFG path, while CH follows the AB123FG pathway. Ni is depicted as a large blue (light) atom and Sn is depicted as a large purple atom.

These observations are fairly consistent for different hydrocarbons and also for different surface terminations of Ni with one exception, that on the low-coordinated sites of Ni, for example the step-edge sites on Ni(2 1 1), the CH* would be less thermodynamically stable than separated C* and H*.

The mechanism of elementary steps shown in Fig. 4 suggests that one can formulate the problem of carbon deactivation in terms of the selectivity associated with the formation of C–O versus C–C bonds on Ni. In order to prevent the carbon-induced deactivation, a catalyst should be able to selectively oxidize C atoms rather than form C–C bonds. Fig. 5 shows the DFT-calculated potential energy surfaces for the oxidation of a C atom and for the attachment of a C atom to a carbon nucleation center (C–C bond formation) on the (1 1 1) surface of Ni and the Sn/Ni surface alloy. The carbon nucleation center was modeled as a collection of carbon atoms on Ni assembled in the geometry corresponding to the lowest energy. The DFT calculations indicate that on Ni(1 1 1) the potential energy surfaces associated with the C–C and C–O bond formation are very similar to each other. On the other hand, on the Sn/Ni surface alloy, as modeled in Fig. 5, the overall activation barrier for the C atom oxidation is much lower than the overall activation barrier for the C–C bond formation. The change in the overall activation barrier is a consequence of the increased barrier for the diffusion of C atoms on the Sn/Ni surface alloy. Similar conclusions were obtained for the diffusion of CH* fragment on these surfaces. The DFT-calculated potential energy surface for the diffusion of CH* and O*

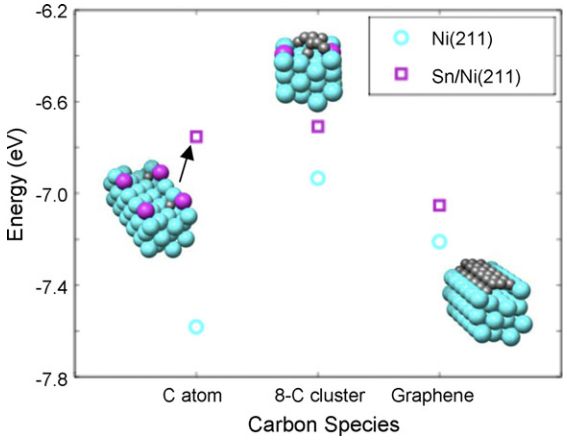

Fig. 7. DFT-calculated adsorption energies per carbon atom for a C atom, C_8 cluster, and a graphene chain adsorbed on Ni(2 1 1) and Sn/Ni(2 1 1). More negative energies suggest more exothermic adsorption process.

on Ni(1 1 1) and Sn/Ni(1 1 1) model alloy are shown in Fig. 6. It is clear that, in contrast to Ni(1 1 1), the barrier for the diffusion of CH* on the Sn/Ni surface alloy is significantly larger that the barrier for the diffusion of O*. These DFT studies indicated that on the Sn/Ni surface alloy, as opposed to monometallic Ni, the oxidation of carbon is kinetically preferred compared to the formation of C–C bonds.

DFT calculations have also demonstrated that in addition to the enhanced capacity to oxidize C atoms, the Sn/Ni surface alloy also lowers the thermodynamic driving force associated with the formation of carbon nucleation centers at the low-coordinated Ni sites. We note that recent in situ TEM studies and DFT calculations have shown that carbon nucleates on low-coordinated Ni sites [17]. DFT calculated adsorption energies for various carbon nucleation centers (a carbon atom, a cluster of eight carbon atoms, and a graphene chain) on monometallic Ni and Sn/Ni surface alloy are shown in Fig. 7. The figure shows that for all carbon structures, the under-coordinated sites on Ni (to model these sites, the Ni(2 1 1) surface was used) bind carbon more strongly than the under-coordinated sites on Sn/Ni(2 1 1). The reason for this is that Sn atoms break the ensembles of low-coordinated Ni sites, which interact strongly with carbon, therefore lowering the propensity of these sites to nucleate extended carbon networks.

5. Conclusion

We showed that Sn/Ni/YSZ catalyst is more carbon-tolerant than Ni/YSZ in steam reforming of isooctane at moderate S/C ratios, irrespective of the average size of metal particles and the metal loading. Our DFT calculations have suggested that the reasons for the enhanced carbon-tolerance of Sn/Ni compared to monometallic Ni are: (i) high propensity of Sn/Ni to oxidize carbon and (ii) lower driving force to form carbon deposits on low-coordinated metal sites.

Acknowledgements

We gratefully acknowledge the support of DOE-NETL (FC26-05-NT-42516 and FC26-06NT42813), DOE-BES, Division of Chemical Sciences (FG-02-05ER15686), and DOE FG02-06CH11300. Supercomputing time at SDSC and Dr. Kai Sun's help with electron microscopy is greatly appreciated.

References

[1] E. Achenbach, E. Riensche, J. Power Sources 52 (1994) 283–288.
[2] A. Atkinson, S. Barnett, R.J. Gorte, J.T.S. Irvine, A.J. Mcevoy, M. Mogensen, S.C. Singhal, J. Vohs, Nat. Mater. 3 (2004) 17–27.
[3] A.L. Dicks, K.D. Pointon, A. Siddle, J. Power Sources 86 (2000) 523–530.
[4] A. Lashtabeg, S.J. Skinner, J. Mater. Chem. 16 (2006) 3161–3170.
[5] J.R. Rostrup-Nielsen, J.B. Hansen, S. Helveg, N. Christiansen, A.K. Jannasch, Appl. Phys. A: Mater. Sci. Process. 85 (2006) 427–430.
[6] J. Mukherjee, S. Linic, J. Electrochem. Soc. 154 (2007) B919–B924.
[7] J.R. Rostrup-Nielsen, Catalytic steam reforming, Catalysis-Science and Technology, vol. 5, Springler, Berlin, 1984.
[8] J.R. Rostrup-Nielsen, J. Sehested, J.K. Norskov, Adv. Catal. 47 (47) (2002) 65–139.
[9] J.M. Wei, E. Iglesia, J. Catal. 224 (2004) 370–383.
[10] H. Timmermann, D. Fouquet, A. Weber, E. Ivers-Tiffee, U. Hennings, R. Reimert, Fuel Cells 6 (2006) 307–313.
[11] F. Abild-Pedersen, J.K. Norskov, J.R. Rostrup-Nielsen, J. Sehested, S. Helveg, Phys. Rev. B 73 (2006).
[12] J.R. Rostrup-Nielsen, Phys. Chem. Chem. Phys. 3 (2001) 283–288.
[13] J.R. Rostrup-Nielsen, T.S. Christensen, I. Dybkjaer, Recent Adv. Basic Appl. Aspects Ind. Catal. 113 (1998) 81–95.
[14] J.R. Rostrup-Nielsen, J. Catal. 85 (1984) 31–43.
[15] J.R. Rostrup-Nielsen, L.J. Christiansen, Appl. Catal. A: Gen. 126 (1995) 381–390.
[16] F. Abild-Pedersen, O. Lytken, J. Engbaek, G. Nielsen, I. Chorkendorff, J.K. Norskov, Surf. Sci. 590 (2005) 127–137.
[17] S. Helveg, C. Lopez-Cartes, J. Sehested, P.L. Hansen, B.S. Clausen, J.R. Rostrup-Nielsen, F. Abild-Pedersen, J.K. Norskov, Nature 427 (2004) 426–429.
[18] D.L. Trimm, Catal. Today 37 (1997) 233–238.
[19] D.L. Trimm, Catal. Today 49 (1999) 3–10.
[20] H.S. Bengaard, J.K. Norskov, J. Sehested, B.S. Clausen, L.P. Nielsen, A.M. Molenbroek, J.R. Rostrup-Nielsen, J. Catal. 209 (2002) 365–384.
[21] T. Takeguchi, Y. Kani, T. Yano, R. Kikuchi, K. Eguchi, K. Tsujimoto, Y. Uchida, A. Ueno, K. Omoshiki, M. Aizawa, J. Power Sources 112 (2002) 588–595.
[22] N.C. Triantafyllopoulos, S.G. Neophytides, J. Catal. 217 (2003) 324–333.
[23] C.M. Finnerty, N.J. Coe, R.H. Cunningham, R.M. Ormerod, Catal. Today 46 (1998) 137–145.
[24] R.M. Watwe, H.S. Bengaard, J.R. Rostrup-Nielsen, J.A. Dumesic, J.K. Norskov, J. Catal. 189 (2000) 16–30.
[25] I. Alstrup, M.T. Tavares, C.A. Bernardo, O. Sorensen, J.R. Rostrup-Nielsen, Mater. Corros. 49 (1998) 367–372.
[26] X.Y. Chen, A.R. Tadd, J.W. Schwank, J. Catal. 251 (2007) 374–387.
[27] J. Xu, M. Saeys, J. Catal. 242 (2006) 217–226.
[28] E. Nikolla, A. Holewinski, J. Schwank, S. Linic, J. Am. Chem. Soc. 128 (2006) 11354–11355.
[29] F. Besenbacher, I. Chorkendorff, B.S. Clausen, B. Hammer, A.M. Molenbroek, J.K. Norskov, I. Stensgaard, Science 279 (1998) 1913–1915.
[30] N. Nichio, M.L. Casella, G.F. Santori, E.N. Ponzi, O.A. Ferretti, Catal. Today 62 (2000) 231–240.
[31] O. Sidjabat, D.L. Trimm, Top. Catal. 11 (2000) 279–282.
[32] J.W. Shabaker, G.W. Huber, J.A. Dumesic, J. Catal. 222 (2004) 180–191.
[33] J.W. Shabaker, D.A. Simonetti, R.D. Cortright, J.A. Dumesic, J. Catal. 231 (2005) 67–76.
[34] J.J. Strohm, J. Zheng, C.S. Song, J. Catal. 238 (2006) 309–320.
[35] R.J. Gorte, J.M. Vohs, J. Catal. 216 (2003) 477–486.
[36] H. Kim, C. Lu, W.L.G. Worrell, R.J.J.M. Vohs, J. Electrochem. Soc. 149 (2002) A247–A250.
[37] I. Ul-Haque, D.L. Trimm, Process for Steam Reforming of Hydrocarbons, Haldor Topsoe, 1997.
[38] E. Nikolla, J. Schwank, S. Linic, J. Catal. 250 (2007) 85–93.
[39] J. Perdew, in: P. Ziesche, H. Eschrig (Eds.), Electronic Structure of Solids '91, Akademie Verlag, Berlin, 1991, pp. 11–20.
[40] J.P. Perdew, Phys. Rev. B: Condens. Matter 33 (1986) 8822.
[41] D. Vanderbilt, Phys. Rev. B 41 (1990) R7892.
[42] J. Rostrup-Nielsen, J.K. Norskov, Top. Catal. 40 (2006) 45–48.
[43] B.D. Gould, X.Y. Chen, J.W. Schwank, J. Catal. 250 (2007) 209–221.